International Journal of Nanomedicine

Dovepress
Taylor & Francis Group

Open Access Full Text Article

ORIGINAL RESEARCH

Nano-Emulsion Incorporating Squalene and Mn^{2+} Stabilized by TA/Mn^{2+} Networks Enhances Subunit Vaccine Immunogenicity

Kai Chen[1], Linlin Li[1], Ning Wang[1], Yunfeng Deng[1], Chuanying Xiang[1], Xiaomin Zhang[1], Yangyang Zhou[1], Hong Yang[1], Yu Xie[1], Xiaoting Chen[2], Ying Li[3], Yan Li[1], Gang Guo[1], Yun Shi[1]

[1]Institute of Biopharmaceuticals, West China Hospital, Sichuan University, Chengdu, Sichuan, People's Republic of China; [2]Animal Experimental Center, West China Hospital, Sichuan University, Chengdu, Sichuan, People's Republic of China; [3]West China School of Pharmacy, Sichuan University, Chengdu, Sichuan, People's Republic of China

Correspondence: Yun Shi, Email shiyun@wchscu.cn

Background: Effective protection against infections requires humoral and cellular immune responses. Although current subunit vaccines primarily induce antibodies, they often fail to elicit strong $CD8^+$ T cell responses. To overcome this challenge, we designed a dual-adjuvant nano-emulsion that integrates squalene (Sq) and Mn^{2+}, using tannic acid (TA)/Mn^{2+} coordination networks for stabilization, serving as a potent immune-enhancing adjuvant system.

Methods: The ultrasonic emulsification was used to prepared nano-emulsion system (Sq@TA/Mn) combining Sq and Mn^{2+}. The Sq@TA/Mn adsorbed ovalbumin (OVA) to form a Sq@TA/Mn@OVA vaccine. The cytotoxicity, ROS generation, cellular uptake, and distribution of the OVA vaccine were evaluated in DC2.4 cells. The retention of OVA vaccines in the site of injection of female C57BL/6 mice were studied using an imaging system. The mice were administered intramuscular injections of Sq@TA/Mn@OVA vaccine with prime-boost immunization strategies. The humoral immune and cellular immune responses were analysed with enzyme-linked immunosorbent assay (ELISA) and flow cytometry, respectively. We evaluated the nano-emulsion using a recombinant peptidoglycan-associated lipoprotein (rPal) antigen to create a Sq@TA/Mn@rPal vaccine against Acinetobacter baumannii-induced pneumonia.

Results: The Sq@TA/Mn nano-emulsion was constructed through ultrasonic emulsification. The nano-emulsion efficiently adsorbed OVA to form a Sq@TA/Mn@OVA vaccine. The OVA vaccine exhibited a favorable safety profile, enhanced ROS generation, dendritic cell uptake, and improved antigen retention at the injection site. Compared to Alum, this vaccine enhanced the production of OVA-specific antibodies and IFN-γ, promoted the expansion of spleen effector memory T cells, and increased the population of lung-resident memory T cells.The Sq@TA/Mn adjuvant elicited higher rPal-specific IgG, IgG1, and IgG2a titers and improved the protective efficacy against infection as compared with Alum.

Conclusion: This study provides a novel method for the co-delivery of Mn^{2+}, Sq, and antigens. These results highlighted the potential of the Sq@TA/Mn platform as a versatile and effective adjuvant for enhancing subunit vaccines.

Keywords: nano-emulsion, Tannic acid/Mn^{2+} networks, adjuvant, vaccine, infection

Introduction

Effective defense against infections, such as, tuberculosis, malaria, and those caused by *Acinetobacter baumannii (A. baumannii*), requires both humoral immunity to halt pathogen spread in the blood and cellular immunity to eradicate infected cells.[1] The evolution of vaccine technology has transformed from traditional inactivated and attenuated vaccines to safer recombinant protein and protein subunit vaccines. However, these vaccines often fail to stimulate robust immune responses.[2,3] Recent subunit vaccines predominantly trigger antibodies, they lack in eliciting $CD8^+$ T cell response.[4,5] Therefore, effective adjuvant delivery systems are required for enhancing the cellular immune response by subunit vaccines.[6,7]

Received: 7 May 2025
Accepted: 7 September 2025
Published: 18 September 2025

Graphical Abstract

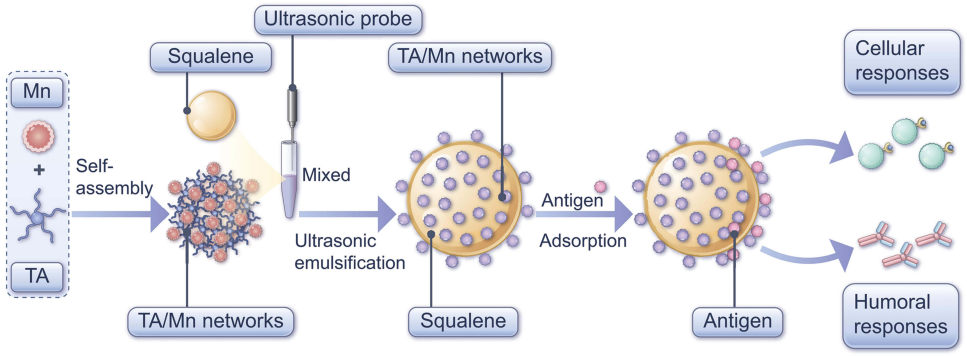

Generally, various pathogen-associated molecular patterns activate multiple pattern recognition receptors in immune cells,[8] thereby triggering robust innate and adaptive immune responses.[9] Manganese (Mn^{2+}) is notable for its potent immunostimulatory properties via activation of the STING pathway. However, its clinical use has been limited by issues related to its pharmacokinetics and potential neurotoxicity.[10] Compared to free Mn^{2+}, a colloidal manganese salt (MnJ) adjuvant significantly enhances the cellular immune response.[11] Mn-based adjuvants have demonstrated the ability to activate innate immunity and improve T cell responses in various preclinical vaccine models.[12,13] Further more, the combination Mn with other immunostimulants may enhance immune response.[14–16]

High levels of reactive oxygen species (ROS) promote dendritic cell maturation and activate downstream innate immune responses.[17] However, the reliance on a single immunostimulatory agent is often insufficient.[14] Squalene (Sq), a Food and Drug Agency-approved drug with a favorable safety profile, increases ROS levels in dendritic cells, facilitating antigen internalization and antigen-presenting cell (APC) activation.[18] Additionally, Sq has been widely used in vaccine research as an oil-in-water emulsion adjuvant to enhance immune responses, including in influenza and COVID-19 vaccines.[19,20] Usually, Sq is recognized as an effective scavenger of singlet oxygen ($^1O_2$) and other ROS.[21] In pro-oxidant environments, Sq can readily undergo peroxidation.[22] This oxidation process itself generates primary ROS (eg, •OH, $O_2•^-$) and leads to the formation of Sq hydroperoxides (SQOOH). These unstable SQOOH can further decompose, producing secondary ROS and reactive aldehydes, thereby amplifying oxidative stress.[22] This phenomenon of Sq acting as a pro-oxidant and ROS inducer under specific circumstances has been documented.[23,24]

Based on these characteristics, we hypothesized that combining Mn^{2+} with Sq might improve the immunomodulatory effects and induce stronger immunity by subunit vaccines. However, the potential synergy between Mn^{2+} and Sq remains unclear. Furthermore, mature APCs exposed to adjuvants exhibit reduced antigen uptake efficiency, which hinders the activation of T cell-mediated humoral and cellular immunity.[25] Thus, the co-delivery of antigens and adjuvants to APCs is crucial for stimulating robust immunity.[25,26]

Notably, the co-delivery of Mn^{2+}, squalene and antigens to APCs is difficult. To address these challenges, we explored tannic acid (TA), which can form metal-phenolic networks (MPNs) with Mn^{2+}. TA binds to proteins through noncovalent interactions, allowing it to interact with proteins of various molecular weights and isoelectric point.[27] Additionally, owing to its strong adsorption capacity, MPNs can self-assemble at the oil-water interface, successfully stabilizing emulsions.[28] Several studies have shown that TA can promote antigen adsorption and facilitate the maturation of dendritic cells, leading to enhanced antigen presentation and immune activation.[29,30] Accordingly, we used the TA/Mn network as an emulsifier to prepare a nano-emulsion with Sq using ultrasonication. Using this emulsion, the protein antigens were physically adsorbed onto the MPN surface, achieving the co-delivery of Mn, Sq, and protein antigens to APCs. Initially, ovalbumin (OVA) was used as a model antigen to characterize the physicochemical properties of the Sq@TA/Mn@OVA vaccine (Figure 1A). Cellular uptake, subcellular localization, distribution, and ROS generation were

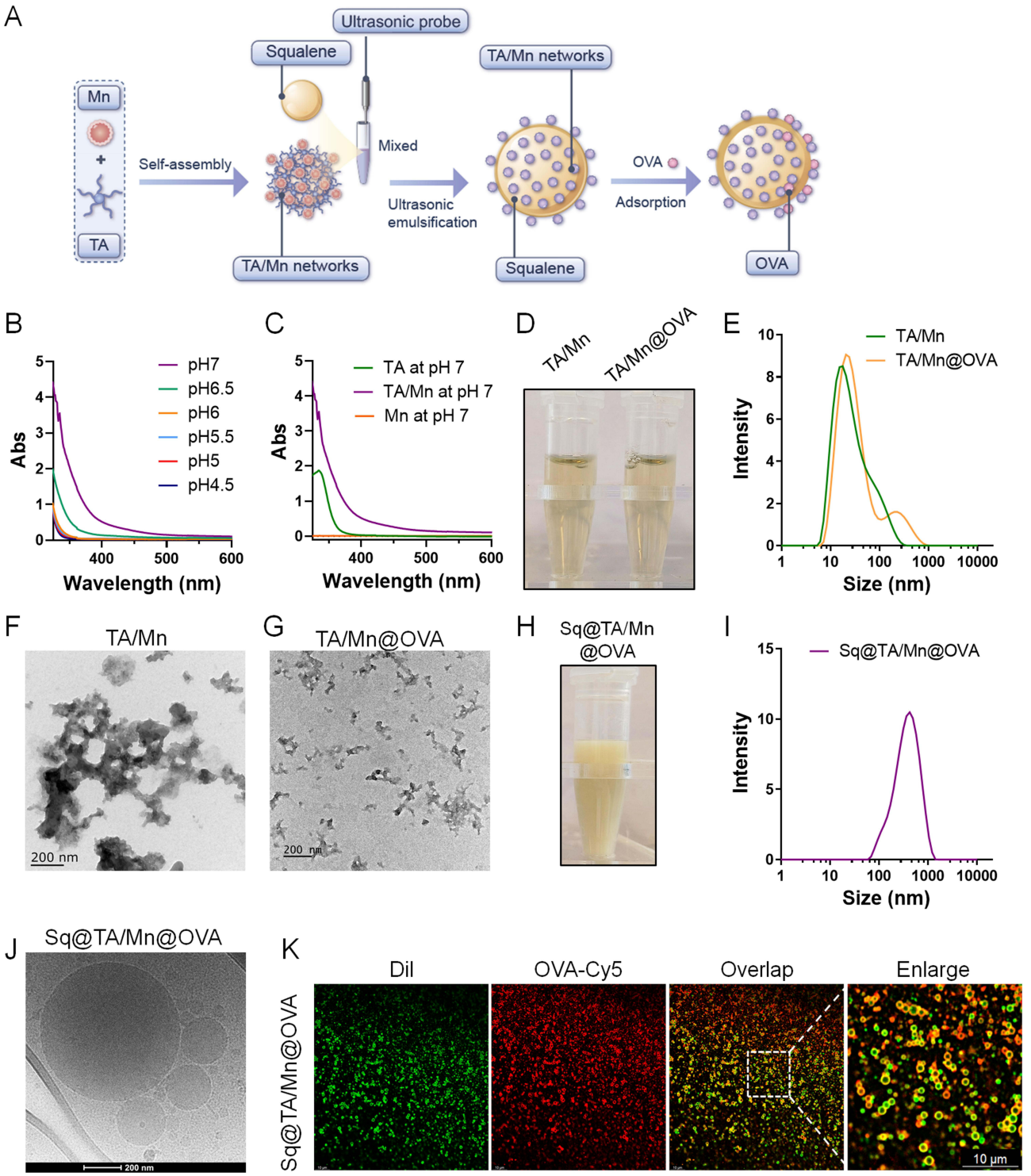

Figure 1 Nano-emulsion prepared via TA/Mn networks as a vaccine adjuvant. (**A**) Rational design of nano-emulsion stabilized by TA/Mn networks for adsorption and delivery of OVA. (**B**) Ultraviolet to visible absorption spectra of TA/Mn networks at various pH values. (**C**) Ultraviolet to visible absorption spectra of TA, Mn and TA/Mn networks at pH 7. (**D**) Photograph of TA/Mn and TA/Mn@OVA. (**E**) Histogram showing the hydrodynamic size of TA/Mn and TA/Mn@OVA analyzed using dynamic light scattering (DLS). TEM image of TA/Mn (**F**) and TA/Mn@OVA (**G**). The scale bar is 200 nm. (**H**) Photograph of and Sq@TA/Mn@OVA nano-emulsion. (**I**) Histogram showing the hydrodynamic size of Sq@TA/Mn@OVA. (**J**) Cryogenic transmission electron microscopy (cryo-TEM) image of Sq@TA/Mn@OVA nano-emulsion. The scale bar is 200 nm. (**K**) STED microscopy image of Sq@TA/Mn@OVA showing the distribution of OVA in the nano-emulsion based vaccine. Scale bar, 10 μm. For the fluorescence image of nano-emulsion based vaccine, OVA was labeled with Cy5 (represented as red) and squalene was labeled with DiI (represented as green).

https://doi.org/10.2147/IJN.S538737

evaluated using fluorescence microscopy. Additionally, we assessed biocompatibility, antigen residency, humoral immune response potency, and specific T cell activation. Finally, we incorporated recombinant peptidoglycan-associated lipoprotein (rPal)[31] from *A. baumannii* into the Sq@TA/Mn nano-emulsion to create the Sq@TA/Mn@rPal vaccine and conducted further studies to assess its protective efficacy. The Sq@TA/Mn platform we constructed show great promise as a versatile and effective adjuvant for enhancing subunit vaccines.

Materials and Methods

Materials

TA, Sq, and dichlorofluorescein diacetate (DCFH-DA) were purchased from Sigma-Aldrich. $MnCl_2$•$4H_2O$, fluorescein isothiocyanate (FITC), and dimethyl sulfoxide were purchased from Macklin (Shanghai, China). Cell counting kit (CCK)-8 was purchased from MedChemExpress (New Jersey, USA). Dulbecco's modified Eagle's medium (DMEM), Roswell Park Memorial Institute (RPMI) 1640 medium, penicillin-streptomycin, and Dulbecco's phosphate-buffered saline (PBS) were purchased from Thermo Fisher Scientific. OVA protein with endotoxin levels of <1 EU/mg was purchased from InvivoGen (France).

Preparation and Characterization of Various Formulations

A typical TA/Mn network was synthesized using an aqueous solution composed of 50 μL of TA solution (4 mg/mL), 2.5 μL of $MnCl_2$•$4H_2O$ (36 mg/mL), and 847.5 μL of distilled water. Following thorough mixing, 100 μL of HEPES buffer (100 mM, pH 4.5–7.0) was added to the solution. The resulting mixtures were analyzed at various pH values using a UV-visible spectrophotometer.

Preparation of TA/Mn@OVA or TA/Mn@rPal vaccine: TA solution (50 μL, 4 mg/mL) and $MnCl_2$•$4H_2O$ (2.5 μL, 36 mg/mL) were added into 797.5 μL of pure water, followed by rapid mixing with 100 μL of HEPES buffer solution (100 mM, pH 7) to synthesize the TA/Mn network. Subsequently, 50 μL of OVA or rPal protein solution (2 mg/mL) was added and allowed to adsorb at room temperature for 30 minutes, resulting in 1 mL of TA/Mn@OVA or TA/Mn@rPal vaccine.

Preparation of Sq@TA/Mn@OVA or Sq@TA/Mn@rPal vaccine: To prepare the nano-emulsion, a one-step sonication process (SCIENTZ-IID; total duration, 120 s; interval time, 4 s) was used, with the TA and Mn networks acting as stabilizers. Different ultrasonic power levels (100, 150, 200, 250, and 300 W) were employed to prepare Sq@TA/Mn nano-emulsion. In particular, a typical Sq@TA/Mn nano-emulsion was formulated by combining 50 μL of TA solution (4 mg/mL), 2.5 μL of $MnCl_2$•$4H_2O$ (36 mg/mL), and 785 μL of distilled water. After thorough mixing, 100 μL of HEPES buffer (100 mM, pH 7.0) was added, followed by rapid mixing and addition of 12.5 μL of Sq. The mixture was emulsified using an ultrasonic homogenizer. For the final preparation of the Sq@TA/Mn nano-emulsion, an additional 50 μL of water was added after sonication. For the preparation of the Sq@TA/Mn@OVA or Sq@TA/Mn@rPal vaccine, 50 μL of an OVA protein or rPal protein solution (2 mg/mL) was introduced after sonication at 250 W (Table S1).

Preparation of Alum@OVA or Alum@rPal vaccine: HEPES buffer solution (100 μL, 100 mM, pH 7) was added to 600 μL of pure water. Then, aluminum hydroxide adjuvant (250 μL, aluminum concentration 10 mg/mL, purchased from Croda) was added. Finally, 50 μL of OVA or rPal protein solution (2 mg/mL) was added, resulting in 1 mL of Alum@OVA or Alum@rPal vaccine.

A Nano Zeta Sizer (Malvern) was used to measure the hydrodynamic size and zeta potential of the various preparations. The morphologies and sizes of TA/Mn and TA/Mn@OVA were assessed using transmission electron microscopy (TEM; JEOL JEM F200, Japan). The elemental composition of TA/Mn@OVA was determined using TEM. The morphologies and sizes of Sq@TA/Mn@OVA nano-emulsion were observed by cryogenic transmission electron microscopy (Cryo-TEM, FEI Talos F200C).

Co-Localization Analysis of OVA and Nano-Emulsion

To investigate the adsorption of the OVA protein on the emulsion surface, an Sq@TA/Mn@OVA vaccine labeled with fluorescent molecules was prepared. Sq and OVA were labeled with DiI and Cy5-NHS, respectively. DiI fluorescent dye

was dissolved in squalene to prepare a 2 mg/mL solution, which was then centrifuged at 3000 × g for 5 minutes. The supernatant was collected to obtain DiI-labeled squalene. The emulsion was prepared using 250 W of ultrasound power, following the steps described above. The fluorescence images of the Sq@TA/Mn@OVA vaccine labeled with fluorescent molecules were captured using a stimulated emission depletion (STED) microscope (Leica).

Cell Line and Animal

The immortalized DC2.4 cell line was obtained from Solarbio Biotechnology Co., Ltd. (Beijing, China) and cultured under suitable conditions. Female C57BL/6 mice were purchased from Chengdu Enswell Biotechnology Co. Ltd. All animal studies were conducted in accordance with the Guidelines for the Care and Use of Laboratory Animals of the West China Hospital and the National Research Council's Guide for the Care and Use of Laboratory Animals (2010). All animal experiments were approved by the Animal Ethics Committee of Sichuan University (Approval No. 2019190A).

Measurement of in vitro ROS Levels

The fluorescent dye, DCFH-DA, was used to measure intracellular ROS generation in DC2.4 cells treated with PBS, OVA, TA/Mn@OVA, or Sq@TA/Mn@OVA. After incubation with various preparations for 6 h, the cells were stained for 20 min with DCFH-DA (10 μM). Thereafter, the fluorescence intensity was measured using flow cytometry and images of the stained cells were captured using a fluorescence microscope.

In vivo Fluorescence Imaging

Cy5 (Lumiprobe) was used to label OVA. Eight-week-old female C57BL/6 mice were administered intramuscular injections of different preparations containing OVA-Cy5 (20 μg /dose of OVA). Typical images of treated mice were captured using an imaging system (Spectral Instruments Imaging). The fluorescence intensity at the injection site was detected for eight days using the Spectral Instruments Imaging system.

Enzyme-Linked Immunosorbent Assay (ELISA)

Blood samples were obtained from the tail vein; serum was collected after centrifugation and then stored at −80°C until use. Levels of antibodies specific to OVA and r-Pal were measured using ELISA. Nunc-Immuno Maxisorp™ plates (Fisher Scientific) were coated with 10 μg/mL of OVA or r-Pal in sodium carbonate-bicarbonate buffer (pH 9.6). After four washes, the plates were blocked for 2 h at 37°C. Serial 5-fold dilutions of serum samples (starting at 1:125) were added and the plates were incubated for 2 h at 37°C. Thereafter, the anti-mouse IgG-horse radish peroxidase (HRP), IgG1-HRP, or IgG2a-HRP (Abcam, 1:100,000 in PBST) was added and the plates were incubated at 37° C for 1 h. After washing, the TMB substrate (Abcam) was introduced in the dark and the reaction was stopped using a stop solution (Solarbio). The optical density (OD) value at 450 nm was measured using a Biotek Synergy microplate reader. Antibody titers were calculated as the highest dilution with an OD450 reading at least 2.1 times more than the mean OD450 of the negative control.

Measurement of Immune Cells in the Spleen

On day 30, splenocytes were isolated by mincing and filtering the spleen through 70-mesh cell strainers. Erythrocyte lysis buffer (0.9% ammonium chloride; eBioscience) was then added, followed by washing with RPMI 1640 medium. After the separation, the collected cells (5×10^6) were co-incubated with OVA antigen (1 mg/mL) at 37°C in an atmosphere of 5% CO_2 and 95% humidity. After 15 h of in vitro restimulation, brefeldin-A (0.8 μg per well) was added. The cells were incubated for another 6 h before intracellular cytokine expression was assessed using flow cytometry. The treated cells were collected via centrifugation (500 × g) and stained with fluorescent antibodies against CD3, CD4, CD8, IL4, and IFNγ (Table S2).

In another experiment, the collected splenocytes (1×10^6) were co-incubated with the OVA antigen (1 mg/mL) for 72 h for in vitro restimulation. Thereafter, the treated cells were collected via centrifugation (500 × g) and the supernatants were harvested to determine the cytokine concentration (IFN-γ, IL-4) using ELISA kits (Dakewe Biotech Co., Ltd).

To estimate the population of memory T cells in the spleen, the collected splenocytes (5×10^6) were stained with fluorescent antibodies against CD3, CD4, CD8, CD44, and CD62L (Table S2).

Bacterial Culture and Mouse Pneumonia Model

The *A. baumannii* strain LAC-4, generously provided by Professor Chen,[32] was used in this study. Female C57BL/6 mice (6–8 weeks old) were used for in vivo experiments. For bacterial preparation, *A. baumannii* was cultivated in tryptic soy broth (TSB) at 37°C with gentle shaking for 5 h. The bacterial density was measured at 600 nm (OD600). Subsequently, 7×10^6 colony-forming units (CFU) of *A. baumannii* were intratracheally administered to each mouse, following previously established protocols.[31] Mouse survival was monitored daily for seven consecutive days.

Statistical Analysis

Statistical analyses were performed using GraphPad Prism version 8. Data presentation, sample size, and p-values are provided in the Figure legends. All data are expressed as mean ± SD. One-way analysis of variance (ANOVA) with Tukey's post-hoc test was used for multiple group comparisons, whereas a two-tailed Student's *t*-test was used for comparisons between two groups. Differences were considered statistically significant at $p < 0.05$ (**** $p < 0.0001$, *** $p < 0.001$, ** $p < 0.01$, * $p < 0.05$), with "ns" indicating not significant differences.

Results

Fabrication and Characterization of Nano-Emulsion

Based on the interfacial self-assembly characteristics of the metal phenolic networks (Figure 1A),[33] TA/Mn^{2+}-based networks were constructed via self-assembly with Mn^{2+} and TA. The UV/visible spectra of the TA/Mn^{2+} network presented higher absorbance values at 325–600 nm than those of TA alone, indicating coordination between TA and Mn^{2+}. With a decrease in pH from 7 to 4.5, the absorbance values at 325–600 nm gradually decreased, indicating that the lower the pH value, the lesser was the amount of Mn^{2+} coordinated with TA, suggesting that the coordination between Mn^{2+} and TA was pH-dependent (Figure 1B and C).[34] At low pH levels, most hydroxyl groups become protonated,[35] which may lead to the rapid destabilization of the cross-links and disassembly of the TA/Mn networks.

To examine whether TA/Mn can adsorb OVA protein, we mixed the TA/Mn networks with OVA, resulting in the formation of TA/Mn@OVA nanoparticles. The TA/Mn and TA/Mn@OVA were pale yellow transparent liquids (Figure 1D). The TA/Mn and TA/Mn@OVA nanoparticles exhibited particle sizes of 21.53 nm and 25.76 nm, and surface potentials of −31.65 mV and −26.06 mV, respectively, as determined using dynamic light scattering (DLS) (Figure 1E and Figure S1). TEM observations revealed that that the TA/Mn and TA/Mn@OVA nanoparticles had irregular morphologies and tended to aggregate (Figure 1F and G). TEM elemental mapping confirmed the presence of O, N, S, and Mn in the TA/Mn@OVA nanoparticles, indicating the successful adsorption of the OVA protein by the TA/Mn networks (Figure S2).

Studies have shown that the strong complex formed between TA and Fe^{3+} can be used to crosslink the oil-water interface to form a nano-emulsion, creating a rigid structure on the surface of oil droplets that further prevents their coalescence and aggregation.[28] Building on this, we utilized TA/Mn networks as emulsifying agents to stabilize Sq oil droplets. We examined the effects of various ultrasonic powers on the homogeneity and particle size of the emulsions. The nano-emulsion was prepared via ultrasonic emulsification of a 1.25% Sq (v/v) mixture in water containing TA/Mn networks according to the formula (Table S1). At ultrasonic powers of 100, 150, and 200 W, the emulsions exhibited phase separation and aggregation on the liquid surface after 24 h. The Sq@TA/Mn emulsion, prepared at 250 W and 300 W, was an opaque pale-yellow liquid and remained stable without phase separation after 24 h (Figures S3). DLS analysis showed that the Sq@TA/Mn nano-emulsion prepared at 300 W had a particle size of 313.17 nm and a size distribution of 0.27, while the emulsion prepared at 250 W had a smaller particle size of 305.67 nm and a narrower size distribution of 0.24 (Figure S4). For subsequent experiments, we selected a lower ultrasonic power of 250 W. At 250 W, Sq@TA/Mn had a surface potential of −41.17 mV. The incorporation of OVA did not noticeably alter the color, particle size, or surface potential, with Sq@TA/Mn@OVA appearing as an opaque pale-yellow liquid (Figure 1H and I), exhibiting

a particle size of 308.3 nm and a zeta potential of −43.96 mV (Figure S5). We also measured the particle size and zeta potential of the formulation prepared by adsorbing OVA onto the aluminum hydroxide adjuvant (Alum@OVA), which were 1597.67 nm and 20.84 mV, respectively (Figure S5). As shown in Figure 1J, Cryo-TEM images revealed that Sq@TA/Mn@OVA nano-emulsion droplets were spherical with well-defined, clear boundaries.To test the capacity of the nano-emulsion to adsorb OVA, we allowed Sq@TA/Mn to adsorb the FITC-labeled OVA. The adsorbing efficiency, measured by fluorescence intensity after centrifugation, was 85.02 ± 0.96% within 30 min, which indicating the high protein-adsorbing ability of Sq@TA/Mn. This suggests that the nano-emulsion densely arrays antigens. As the display of multivalent antigens on the surface of nanoparticles can effectively stimulate the immune system,[27,36] Sq@TA/Mn@OVA may enhance the immune response.

Further, we measured the particle size, polydispersity index (PDI), and zeta potential of the Sq@TA/Mn@OVA nano-emulsion at different time points in HEPES under 4 °C or DMEM containing 10% FBS under 37 °C (Figure S6). We found that their physicochemical properties were well maintained for up to 6 days in HEPES under 4 °C. By day 7, the difference in particle size compared with day 0 exceeded 125 nm, indicating a significant increase in size. Also, the PDI increased. In addition, the zeta potential gradually decreased with prolonged storage. These findings indicate that by day 7, changes in the physical or chemical properties of the nano-emulsion may have occurred, leading to instability in maintaining small droplet sizes and partial aggregation of emulsion droplets. In DMEM containing 10% FBS under 37 °C, the particle size of the nano-emulsion was larger in the FBS-containing medium (502.77 nm) than in HEPES buffer (308.3 nm) by day 0. The result suggests that nano-emulsion may absorb FBS proteins from the medium, leading to an increase in droplet size. With prolonged incubation, the particle size gradually increased, accompanied by an increase in PDI and a decrease in zeta potential. By day 7, the nano-emulsion showed an increase in particle size along with an elevated PDI. Nevertheless, the difference in particle size between day 0 and day 7 did not exceed 70 nm, indicating that compared with HEPES buffer, the Sq@TA/Mn@OVA nano-emulsion exhibited better stability in DMEM supplemented with FBS. This enhanced stability is likely due to the stabilizing effect of proteins.[37]

The distribution of adsorbed OVA in Sq@TA/Mn@OVA was further evaluated by labeling OVA and Sq with Cy5 and DiI, respectively. STED microscopy showed that Cy5-labeled OVA surrounded the green Sq oil droplets (Figure 1K). Co-localization analysis revealed a correlation between red and green fluorescence (Figure S7A) and the Pearson's correlation coefficient was 0.794 (Figure S7B). Additionally, Mander's co-localization coefficients were calculated, which included the M1 and M2 values. The M1 value represents the ratio of the red pixels from Cy5-labeled OVA to co-localized green pixels from DiI in Sq, whereas the M2 value corresponds to the ratio of the green pixels from DiI to the co-localized red pixels from Cy5-labeled OVA. The M1 and M2 values for the Sq@TA/Mn@OVA vaccine were 0.75 and 0.79, respectively (Figure S7B). These results suggest that the Sq@TA/Mn nano-emulsion effectively loaded OVA.

Evaluation of Cytotoxicity, ROS Generation, Cellular Uptake, and Distribution of the OVA Vaccines in DC2.4 Cells

To assess the cytotoxicity of various preparations, we performed a CCK-8 assay using DC2.4 cells with an OVA concentration of 25 μg/mL (Figure 2A). No significant cytotoxicity was observed after 6 h of incubation with any of the preparations, indicating good cellular biocompatibility of Sq@TA/Mn@OVA at an OVA concentration of 25 μg/mL and Sq concentration of 3.125 μL/mL. Prolonged incubation to 24 h resulted in a marked decrease in cell viability in both the TA/Mn@OVA and Sq@TA/Mn@OVA groups. This effect is likely attributable to sustained activation of DC2.4 cells, which can lead to high levels of oxidative stress,[38] which triggers cell death. Next, we analyzed the intracellular ROS generation induced by Sq@TA/Mn@OVA using the fluorescent probe, DCFH-DA. As presented in Figure 2B and C, ROS generation was enhanced after incubation with TA/Mn@OVA or Sq@TA/Mn@OVA for 6 h. Sq@TA/Mn@OVA elicited a significant increase in intracellular ROS generation in DC2.4 cells.

The intracellular green fluorescence intensity did not differ considerably between the two groups incubated with PBS or OVA alone for 6 h. The intracellular green fluorescence intensity was considerably stronger in the cells treated with Sq@TA/Mn@OVA than that in cells treated with OVA or TA/Mn@OVA. ROS production in the cells incubated with TA/Mn@OVA was 19.32 times higher than that in the cells incubated with OVA. These results suggest that the

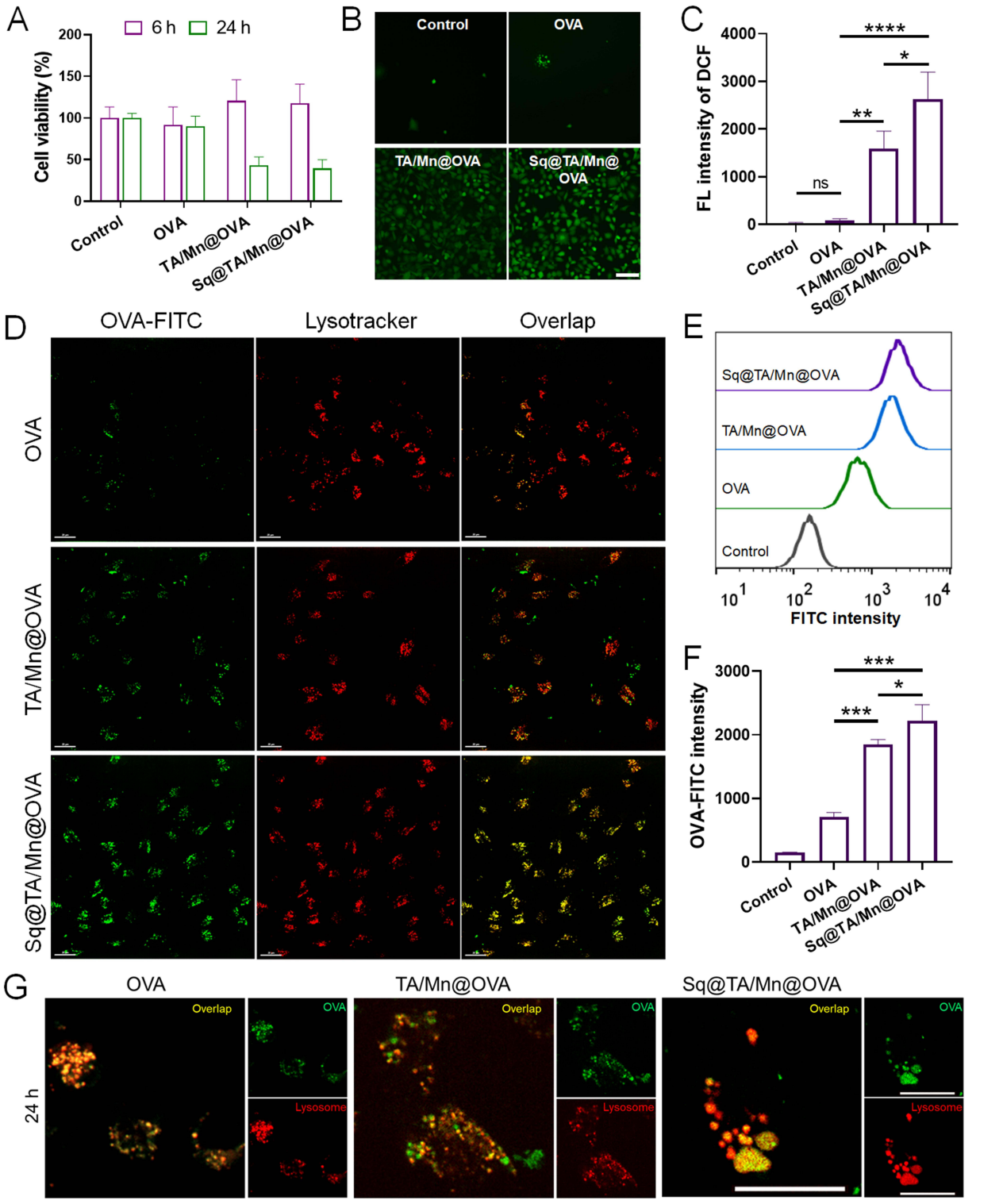

Figure 2 (**A**) CCK-8 assay to assess cytotoxicity of different preparations on DC2.4 cells after 6 h or 24 h incubation with 25 μg/mL OVA and Sq concentration of 3.125 μL/mL. (**B**) Fluorescence images of DC2.4 cells exposed to PBS, OVA, TA/Mn@OVA, or Sq@TA/Mn@OVA at OVA concentration of 75 μg/mL and squalene concentration of 9.375 μL/mL for 6 h. Intracellular ROS generation was detected via DCFH-DA (green: DCF). Scale bar: 100 μm. (**C**) Quantitative measurement of intracellular ROS production in DC2.4 cells incubated with different preparations for 6 h using flow cytometry. Data were presented as mean ± SD (n = 3). (**D**) Confocal laser scanning microscopy (CLSM) images of the various preparations loaded with OVA (green) after treatment with DC2.4 cells for 8 h. OVA was labeled with FITC. LysoTracker Red (red) was used to stain lysosomes. Scale bars, 10 μm. Typical flow cytometry plots (**E**) and quantitative measurement (**F**) of intracellular FITC-labeled OVA accumulation in DC2.4 cells treated with various formulations for 8 h. Data are shown as mean ± SD (n = 3). (**G**) Distribution of FITC-labeled OVA and morphs of LysoTraker Red-labeled lysosome in DC2.4 cell after treatment with different preparations for 24 h visualized using CLSM. Scale bar is 20 μm. * for $p < 0.05$, ** for $p < 0.01$, *** for $p < 0.001$; and **** for $p < 0.0001$. ns, not significant.

introduction of Mn significantly increased ROS generation.[39] Additionally, ROS generation in cells treated with Sq@TA/Mn@OVA was 1.65 times higher than that in cells treated with TA/Mn@OVA. The Sq@TA/Mn@OVA group presented the highest ROS levels among the three preparations owing to the presence of Mn^{2+} and Sq, which indicated that Mn^{2+} and Sq synergistically induced ROS production in DC2.4 cells.

Successful internalization of antigens is important for subsequent activation of APCs and effective antigen presentation.[25] To assess the antigen delivery efficiency of Sq@TA/Mn@OVA, we co-incubated Sq@TA/Mn@OVA labeled with FITC-OVA with DC2.4 cells. OVA and TA/Mn@OVA were also tested (Figure 2D). Compared with OVA and TA/Mn@OVA, Sq@TA/Mn@OVA exhibited increased OVA intercellular concentrations, as the strongest green fluorescence was observed in the Sq@TA/Mn@OVA group. After internalization, co-localization (yellow) of OVA-FITC (green) and lysosomes (Lysotracker Red) was observed in the images shown in Figure 2D, implying that Sq@TA/Mn@OVA could deliver OVA to lysosomes.

Owing to less internalization of OVA, a considerably weaker co-localization signal was observed in the soluble OVA and TA/Mn@OVA groups. To confirm these results, we examined the efficiency of OVA-FITC uptake using flow cytometry. According to Figure 2E and F, Sq@TA/Mn@OVA exhibited higher levels of OVA-FITC internalization than OVA and TA/Mn@OVA. Furthermore, Sq@TA/Mn@OVA significantly enhanced the internalization of OVA by 3.14-fold and 1.21-fold as compared with OVA and TA/Mn@OVA, respectively, indicating that particulate antigens were more readily recognized by dendritic cells, which explains the increased OVA uptake in the TA/Mn@OVA and Sq@TA/Mn@OVA groups. The higher antigen uptake in the Sq@TA/Mn@OVA group was possibly due to its stronger ROS generation, which promoted DC2.4 cell maturation.[40]

Furthermore, we investigated whether the uptake behavior of DC2.4 cells was time-dependent for these three preparations. We observed that the internalization of the three formulations gradually increased with the extension of incubation time (Figure S8). This indicated that the uptake behavior of the three different preparations by DC2.4 cells was time-dependent. Additionally, we extended the incubation time of DC2.4 cells with the three formulations for 24 h and examined the distribution of OVA and morphology of the lysosomes. Upon prolonging the incubation to 24 h, we observed that lysosomes in DC2.4 cells treated with Sq@TA/Mn@OVA swelled, while those in the OVA and TA/Mn@OVA groups did not (Figure 2G). Lysosomal swelling induced by Sq@TA/Mn@OVA may lead to autophagy, facilitating cross-presentation, potentially promoting dendritic cell maturation and activation during immunization.[41] Therefore, these properties of nano-emulsion confer its potential to promote maturation and activation of dendritic cells during the immunization process.

Safety Estimation of the Various OVA Vaccines

To evaluate the biological safety of the Sq@TA/Mn@OVA vaccine, female C57BL/6 mice were intramuscularly injected with HEPES, OVA, TA/Mn@OVA, Sq@TA/Mn@OVA, or Alum@OVA on days 0, 14, and 21. Serum samples were collected on day 30 to determine serum biochemical indices and the major organs were examined for pathological symptoms.

As shown in Figure 3A, no apparent pathologies were observed in the primary organs (heart, liver, spleen, lung, and kidney), suggesting the acceptable biosafety of Sq@TA/Mn@OVA. Moreover, no significant variations in body weight were detected in the OVA, TA/Mn@OVA, Sq@TA/Mn@OVA, or Alum@OVA groups compared with those in the control group (Figure S9). Furthermore, the levels of lactate dehydrogenase (LDH), aspartate aminotransferase (AST), alanine aminotransferase (ALT), alkaline phosphatase (ALP), and blood urea nitrogen (BUN) in the OVA groups remained comparable to those in the control group (HEPES-treated), suggesting minimal adverse effects on the cardiovascular, hepatic, and renal functions (Figure 3B). [42–44] Consequently, the nano-emulsion displayed acceptable biocompatibility as a potential vaccine adjuvant.

Antigen Residency and Humoral Immune Response of Various OVA Vaccines

Prolonging the duration of antigen presence at the injection site can extend APC activation and enhance immune response.[45] The antigen residency at the injection site was detected using an in vivo fluorescent imaging system. Female C57BL/6 mice were treated with various formulations of Cy5-labeled OVA via intramuscular injection. As presented in Figure 4A and B, the fluorescence intensity in the free OVA-Cy5 group disappeared at the site of injection within 72 h. Notably, the fluorescence intensity of Cy5 in the TA/Mn@OVA group lasted for 192 h. Surprisingly, the

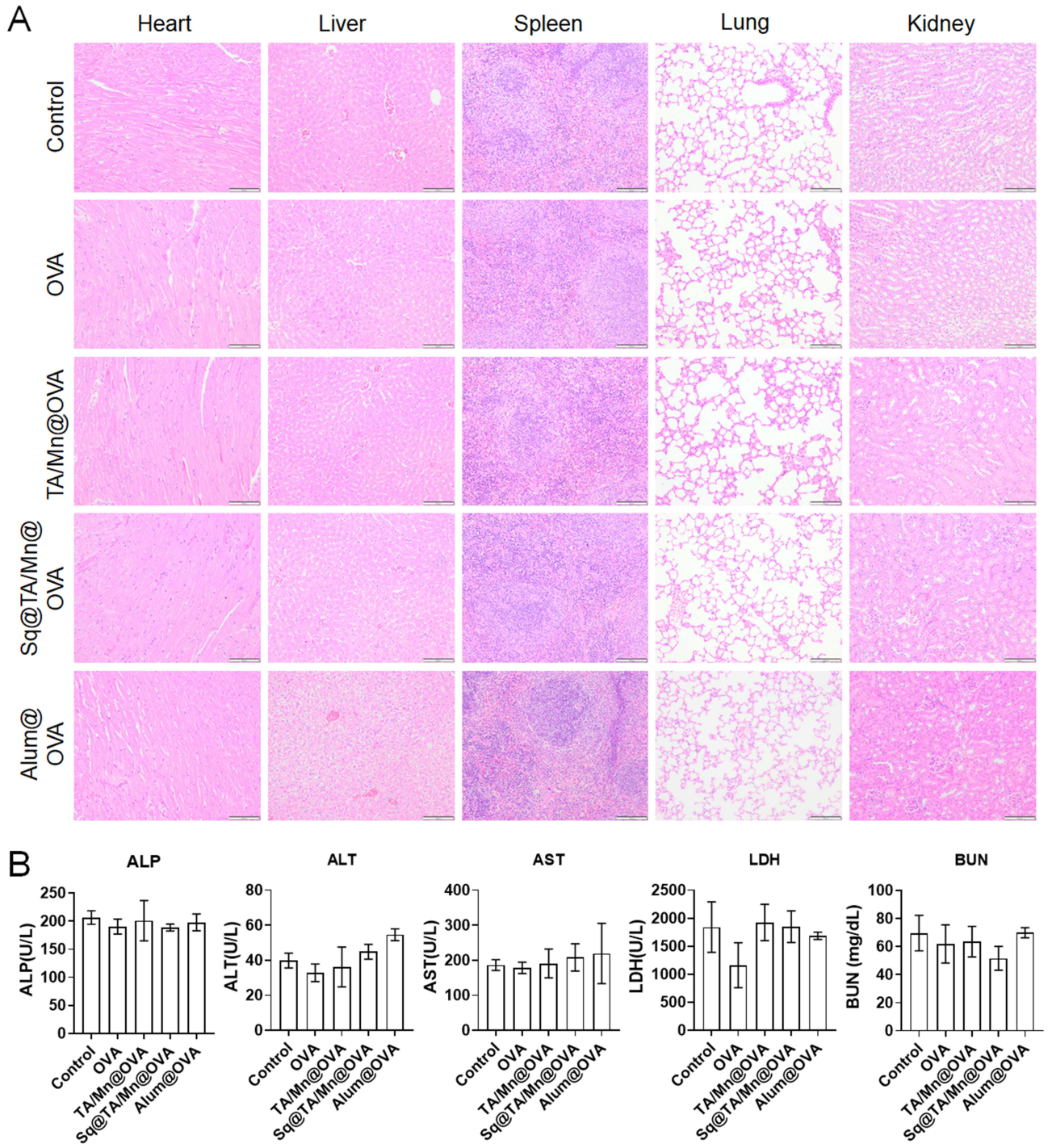

Figure 3 Safety evaluation of various preparations. (**A**) Histological images of hematoxylin-eosin (H–E)-stained organs from mice treated with HEPES, OVA, TA/Mn@OVA, Sq@TA/Mn@OVA or Alum@OVA. Scale bar: 100 μm. (**B**) Serum biochemical parameters following immunization. The levels of ALP, ALT, AST, LDH, and BUN were analyzed. Data were presented as mean ± SD (n = 4). Blood and organs were collected on day 30 after the first immunization.

Sq@TA/Mn@OVA vaccine lasted for over six days at the site of injection. These results suggest that the Sq@TA/Mn@OVA vaccine demonstrates an antigenic depot effect, ensuring sustained vaccine delivery and potentially enhancing the innate immune response at the injection site.

To examine whether Sq@TA/Mn@OVA could effectively induce an enhanced humoral immune response, female C57BL/6 mice were treated with OVA, TA/Mn@OVA, or Sq@TA/Mn@OVA on days 0, 14, and 21 via intramuscular

injection (Figure 4C). On day 30, serum samples were obtained to measure OVA-specific antibody titers. The OVA-specific IgG titer in the Sq@TA/Mn@OVA group was 6.54-fold higher than that in the TA/Mn@OVA group (Figure 4D). The IgG subtype analysis revealed increased levels of IgG1 (Th2-associated) and IgG2a (Th1-associated) after

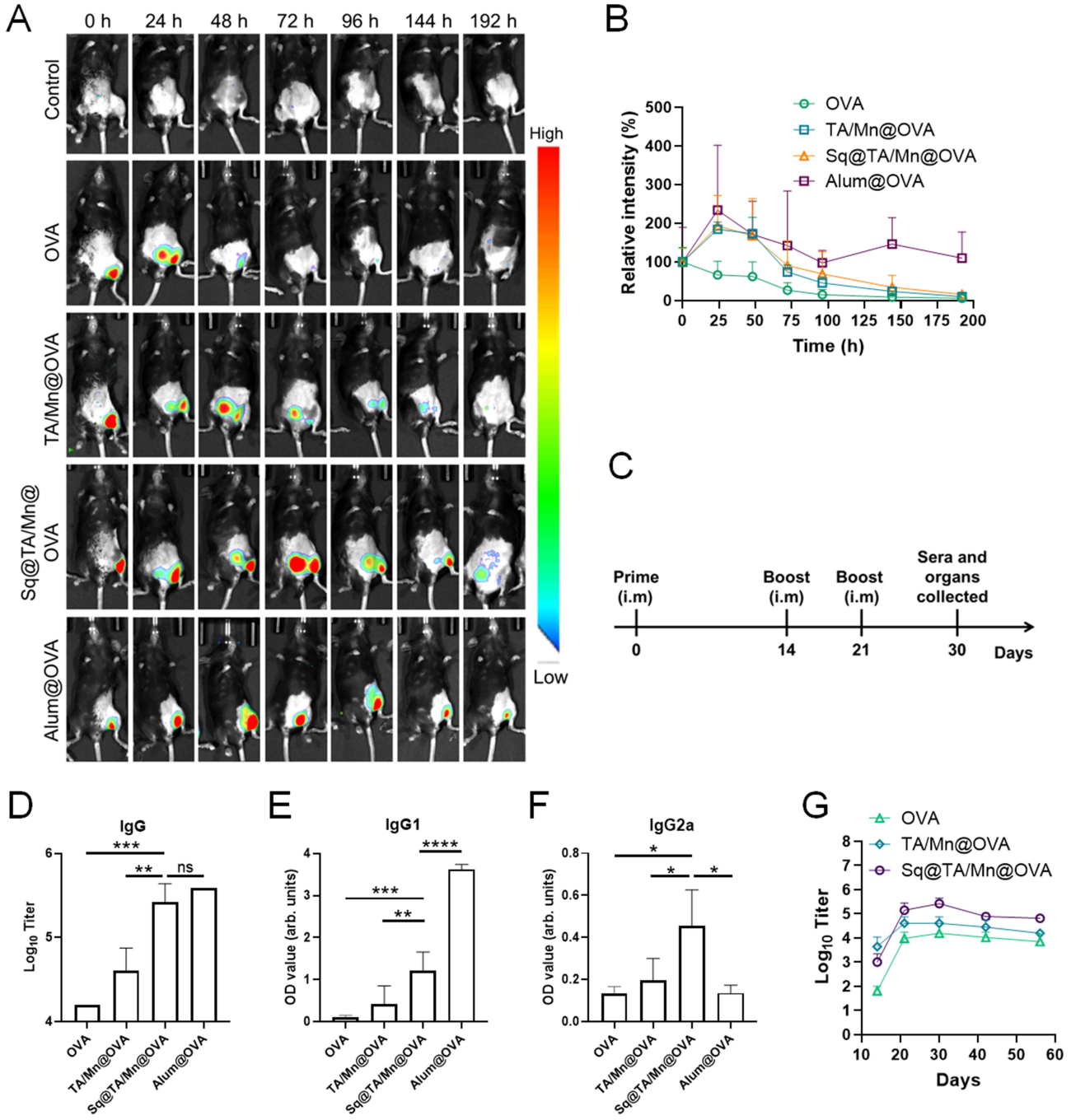

Figure 4 Robust humoral immune response to OVA vaccines. (**A**) Fluorescence intensity of OVA remaining at injection sites was quantified. OVA was tagged with Cy5. Intramuscular injections of various vaccine formulations containing Cy5-labeled OVA were administered into the gluteus maximus of BALB/c mice. Persistence of OVA at injection sites was assessed using an in vivo imaging system at the designated time points (excitation: 648 nm; emission: 662 nm). (**B**) Quantification of total fluorescence intensity at sites of injection using an imaging software. Results are shown as mean ± SD (n = 4). (**C**) A schematic representation of the immunization protocol and overall experimental setup is shown. Each group of five mice was immunized on days 0, 14, and 21 with either OVA, TA/Mn@OVA, Sq@TA/Mn@OVA, or Alum@OVA. Serum samples were collected on day 30 for determination of total IgG (**D**), IgG1 (**E**), and IgG2a (**F**) titers against OVA. E and F were performed at 1:15625 and 1:625 dilutions, respectively. In panels D, E, and F, data are also presented as mean ± SD (n = 5). (**G**) The overall anti-OVA IgG titers in mice on days 0, 14, 21, 30, 42, and 56 of mice injected on days 0, 14, and 21 with OVA, TA/Mn@OVA, or Sq@TA/Mn@OVA. Data plotted are presented as mean ± SD (n = 5). The p values are listed in Table S3. Statistical comparisons were performed with a two-tailed unpaired Student's *t*-test, with significance levels of *p < 0.05, **p < 0.01, ***p < 0.001, and ****p < 0.0001. ns, not significant.

https://doi.org/10.2147/IJN.S538737

immunization with Sq@TA/Mn@OVA (Figure 4E and F). Sq@TA/Mn@OVA mediated 2.96-fold and 2.57-fold increases in the OD values of IgG1 and IgG2a compared with TA/Mn@OVA, respectively. Additionally, Sq@TA/Mn@OVA presented higher IgG2a titers than Alum@OVA, which may be ascribed to the enhanced Th1 immune induced by Mn^{2+}.[11] These findings further substantiate the notion that Sq@TA/Mn@OVA elicits a mixed immune response involving both Th1 and Th2 activation, possibly due to the synergistic enhancement of the immune response by Mn^{2+} and Sq.

To monitor changes in total anti-OVA IgG titers over time, serum samples were collected from mice to determine IgG titers on days 14, 21, 30, 42, and 56 after the first immunization (Figure 4G). The OVA-specific IgG titers in the Sq@TA/Mn@OVA group peaked on day 30 after the third injection. Over time, these titers gradually declined in all groups. In comparison to mice vaccinated with OVA or TA/Mn@OVA, mice immunized with Sq@TA/Mn@OVA exhibited significantly higher OVA IgG titers on days 21, 30, 42, and 56 (Figure 4G and Table S3). These results suggest that the combination of Mn^{2+} and Sq can enhance the humoral immune response and maintain antibody titers at relatively high levels over an extended period.

T Cell Responses in the Spleen

The ideal vaccine response is a balanced Th1 and Th2 response that activates cellular and antibody-mediated immune responses.[46] Further, we examined the activation of cellular immunity triggered by OVA vaccines. Splenocytes were collected from vaccinated mice to assess cytokine production upon OVA restimulation. Flow cytometry was used to evaluate the production of IFN-γ (Th1) and IL-4 (Th2) by $CD4^+$ and $CD8^+$ T cells (Figure S10 and S11) to determine the extent of the cellular immune responses.

As indicated in Figure 5A–D, Sq@TA/Mn@OVA was found not only to promote an increase in the secretion of Th1 cytokines (IFN-γ) but also to significantly augment the release of Th2 cytokines (IL-4) in $CD4^+$ and $CD8^+$ T cell populations. Notably, more IFN-γ and IL-4 were detected in the Sq@TA/Mn@OVA group (Figure S12), when splenocytes from different groups were cultured in the presence of 1 mg/mL OVA for 72 h. The IFN-γ level in the Sq@TA/Mn@OVA group was considerably higher than that in the Alum@OVA group, indicating that it induced a stronger Th1-type immune reaction. These data indicate that Sq@TA/Mn@OVA elicits a marked enhancement in immune responses mediated by T cells, distinguished by a mixed Th1 and Th2 immune reaction.

The primary objective of vaccination is to generate an immune memory with the ability to protect the host from pathogenic infections.[47] The longevity of memory immune responses is the foundation for effective vaccination.[48] Long-term immune responses are primarily mediated by memory T cells, which include central memory T cells ($CD44^+CD62L^+$) and effector memory T cells ($CD44^+CD62L^-$), both playing crucial roles in this process.[49] Effector memory T cells provide immediate defense against re-exposure to pathogens.[49] To assess the capacity of different vaccine formulations to induce memory T cells, we compared the percentages of memory cells within both $CD4^+$ and $CD8^+$ T cell populations (Figure S13). Notably, the Sq@TA/Mn@OVA vaccine significantly expanded the effector memory T cell population ($CD44^+CD62L^-$), comprising 25.8% of $CD4^+$ T cells and 20.88% of $CD8^+$ T cells in the spleens of treated mice (Figure 5E–J). In contrast, the effector memory T cell population in the Alum@OVA group exhibited 2.99% of $CD4^+$ and 3.55% of $CD8^+$ T cells (Figure 5E–J). Fluorescence activated cell sorting analysis revealed that the Sq@TA/Mn@OVA nano-emulsion induced a notably higher proportion of effector memory T cells, suggesting a more potent stimulation of cellular immunity. The vaccine successfully induced adaptive immune responses and developed antigen-specific immune memory. These results indicate that the Sq@TA/Mn@OVA vaccine not only elicits a stronger cellular immune response but also promotes the formation of effector memory T cells. This enhanced immune memory response may be attributed to the synergistic immunostimulatory effects of Mn^{2+} and squalene, which together drive a robust and sustained immune memory.[50]

T Cell Responses in the Lungs

Resident memory T cells (TRM) within the lung tissue have been demonstrated to occupy strategic locations at sites of pathogen entry, where they perform crucial functions in front-line defense against viral and bacterial infections through direct interaction with invading pathogens.[51] To evaluate T cell responses in the lungs, mice vaccinated via intramuscular

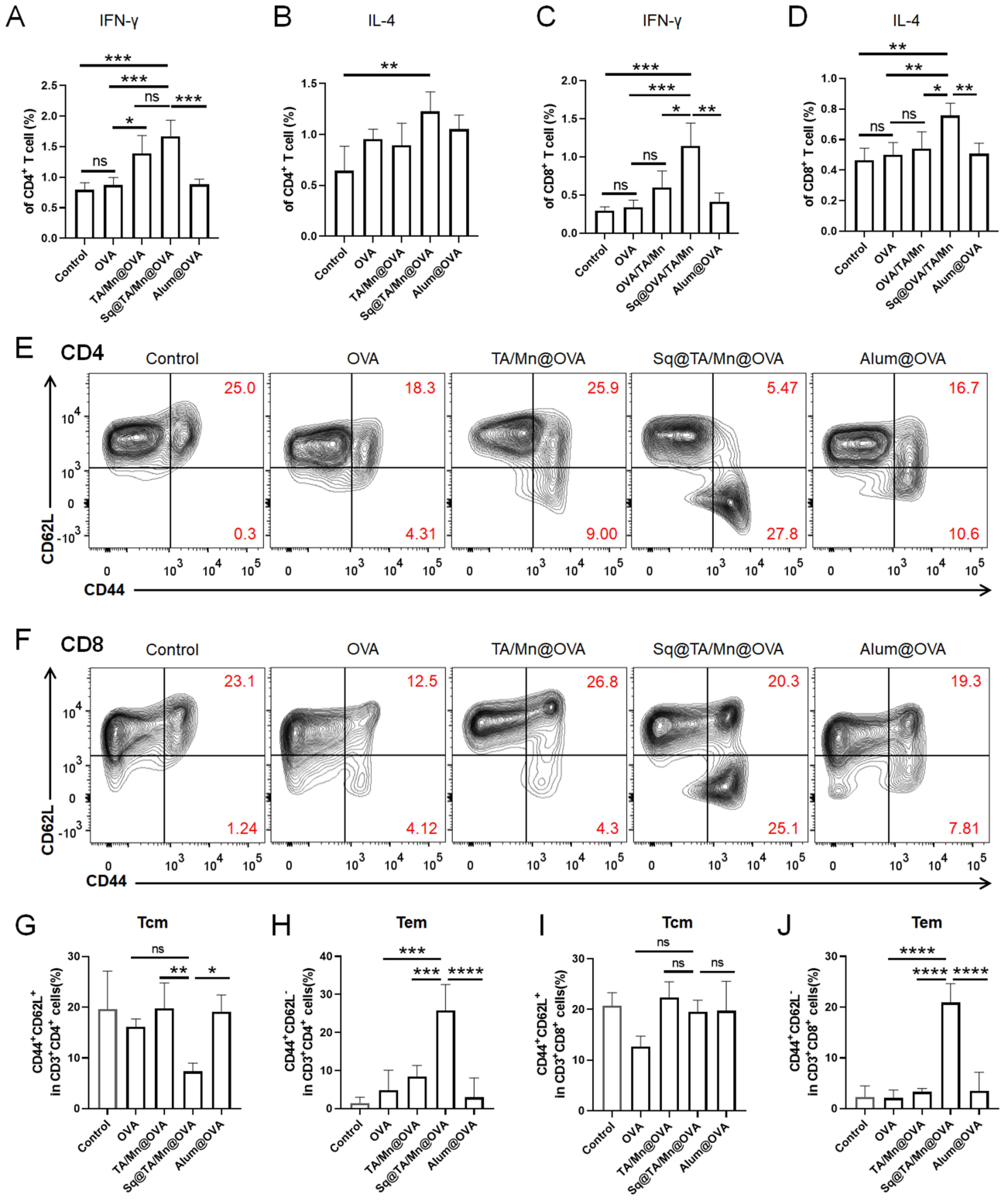

Figure 5 The OVA vaccines induced cellular immunity. (**A**) Frequency of IFN-γ secretion by $CD4^+$ T cells. (**B**) Frequency of IL4 secretion by $CD4^+$ T cells. (**C**) Frequency of IFN-γ secretion by total $CD8^+$ T cells. (**D**) Frequency of IL4 secretion by $CD8^+$ T cells. Typical flow cytometry plots of $CD4^+$ (**E**) and $CD8^+$ (**F**) T cell central memory and effector memory phenotypes in the spleen. The red numbers represent the percentage of cells in certain quadrants. Frequency of central memory (Tcm) $CD4^+$ ($CD44^+CD62L^+$) (**G**) and effector memory (Tem) $CD4^+$ ($CD44^+CD62L^-$) (**H**) T cells in the spleen. Frequency of central memory $CD8^+$ ($CD44^+CD62L^+$) (**I**) and effector memory $CD8^+$ ($CD44^+CD62L^-$) (**J**) T cells in the spleen. Data are shown as mean ± SD (n = 4). Statistical comparisons were performed using a two-tailed unpaired Student's *t*-test, with significance levels of *p < 0.05, **p < 0.01, ***p < 0.001, and ****p < 0.0001. ns, not significant.

https://doi.org/10.2147/IJN.S538737

injection with HEPES, OVA, TA/Mn@OVA, Sq@TA/Mn@OVA, or Alum@OVA were sacrificed on day 30. The lungs were collected, and T cells were detected using flow cytometry. The gating strategy for the lung T cell data collected using flow cytometry is presented in Figure S14. Notably, the Sq@TA/Mn@OVA vaccine showed 36.15% memory $CD4^+$ T cells (identified as $CD4^+$ $CD44^+$) and 63.25% memory $CD8^+$ T cells (identified as $CD8^+$ $CD44^+$) in the lungs of the

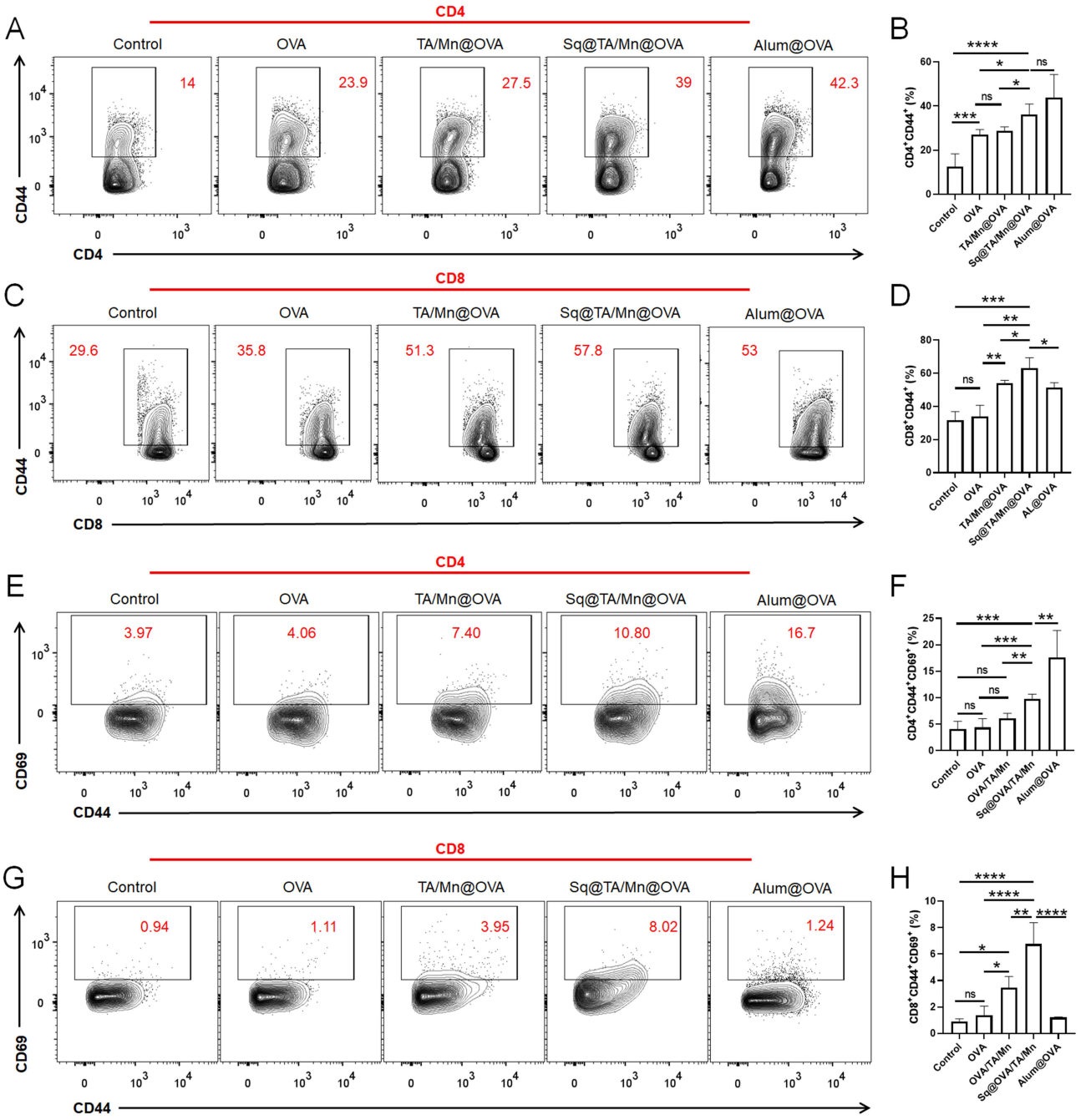

Figure 6 Intramuscular administration of adjuvanted OVA vaccines elicited lung TRM immune reactions. Mice received injections of HEPES, OVA, TA/Mn@OVA, Sq@TA/Mn@OVA, or Alum@OVA on days 0, 7, and 21. On day 30, the immunized mice were euthanized, and their lung tissues were collected. Lung T cell activation was assessed using flow cytometry. Typical flow cytometry plots (**A**) and quantification (**B**) of $CD44^+$ T cells in $CD4^+$ T cells in the lungs of vaccinated mice, respectively. The red numbers represent the percentage of $CD4^+CD44^+$ cells. Typical flow cytometry plots (**C**) and quantification (**D**) of $CD44^+$ T cells in $CD8^+$ T cells in the lungs of vaccinated mice, respectively. The red numbers represent the percentage of $CD8^+CD44^+$ cells. Typical flow cytometry plots (**E**) and quantification (**F**) of CD69 expression in $CD4^+$ $CD44^+$ T cells in the lungs of vaccinated mice, respectively. The red numbers represent the percentage of $CD69^+$ cells in $CD4^+$ $CD44^+$ T cells. Typical flow cytometry plots (**G**) and quantification (**H**) of CD69 expression in $CD8^+$ $CD44^+$ T cells in the lungs of vaccinated mice, respectively. The red numbers represent the percentage of $CD69^+$ cells in $CD8^+$ $CD44^+$ T cells. The data are shown as mean ± SD (n = 4). The data are shown as mean ± SD (n = 4). Statistical comparisons were performed using a two-tailed unpaired Student's *t*-test, with significance levels of *p < 0.05, **p < 0.01, ***p < 0.001, and ****p < 0.0001. ns, not significant.

treated mice (Figure 6A–D). Our observations demonstrated a notable increase in the proportion of memory $CD4^+$ and $CD8^+$ T cells within the lungs of mice that received the Sq@TA/Mn@OVA vaccine compared with those that were administered HEPES, OVA, TA/Mn@OVA, or Alum@OVA (Figure 6A–D). Additionally, the expression of CD44 and CD69 in T cells was used as a marker to identify lung TRM cells.[52] Following Sq@TA/Mn@OVA immunization, lung memory $CD4^+$ and $CD8^+$ T cells exhibited considerably higher expression of the tissue-resident marker, CD69. In contrast, memory $CD4^+$ and $CD8^+$ T cells induced by vaccination with HEPES, OVA, TA/Mn @OVA, or Alum@OVA displayed significantly lower expression frequencies of this marker (Figure 6E–H). The data presented suggests that intramuscular administration of an OVA vaccine in conjunction with the Sq@TA/Mn adjuvant leads to enhanced and sustained $CD4^+$ and $CD8^+$ TRM cell responses within the lungs. Previous studies have established that $CD8^+$ TRM cells in the lungs are essential for triggering heterosubtypic protection against respiratory pathogens. Upon re-exposure to pathogens, T cells provide swift and efficient immune protection.[53] Consequently, the establishment of $CD8^+$ TRM cells following intramuscular vaccination with a nano-emulsion indicates the potential for long-lasting protection against lung infections when combined with appropriate immunogens.

Protective Efficiency of rPal Vaccine Based on Sq@TA/Mn Against Pulmonary A. baumannii Infection

Motivated by the strong humoral and cellular immune responses elicited by the Sq@TA/Mn@OVA vaccine, we evaluated the protective efficacy of the Sq@TA/Mn nano-emulsion in combination with a bacterial antigen from *A. baumannii*, a gram-negative coccobacillus responsible for nosocomial infections such as septicemia and pneumonia.[54]

Previously, we have identified Pal as a potential vaccine candidate; however, when rPal was administered with an aluminum adjuvant to C57BL/6 mice, the resulting protective efficacy was limited to 40%.[31] To determine whether the Sq@TA/Mn nano-emulsion adjuvant can enhance the protective efficacy of the rPal-based vaccine, we first prepared various rPal vaccines using a method similar to that described above. TA/Mn@rPal, Sq@TA/Mn@rPal, and Alum@rPal exhibited particle sizes of 33.91 nm, 341.67 nm, and 1301.67 nm, respectively (Figure 7A). The zeta potentials of TA/Mn@rPal, Sq@TA/Mn@rPal, and Alum@rPal were −25.83 mV, −33.61 mV, and 25.83 mV, respectively (Figure 7B). The loading efficiency of Sq@TA/Mn nano-emulsion for rPal was 94.03 ± 0.45%. These results indicated that the Sq@TA/Mn nano-emulsion could adsorb different antigens, demonstrating a certain level of versatility. Subsequently, we immunized the mice on days 0, 14, and 21 with various rPal vaccines (Figure 7C). On day 30, blood was collected from the tail vein to measure antibody titers. Compared with the group immunized with Alum@rPal, the group receiving Sq@TA/Mn@rPal exhibited significantly elevated levels of total IgG, as well as IgG1 and IgG2a (Figure 7D–F).

On day 33, the immunized mice were intratracheally challenged with a virulent strain of *A. baumannii*. The control groups receiving HEPES showed 100% mortality, whereas 20% of the mice immunized with Alum@rPal survived the infection. In contrast, 80% of the mice immunized with Sq@TA/Mn@rPal survived the infection (Figure 7G). These findings clearly demonstrated that the Sq@TA/Mn nano-emulsion adjuvant significantly enhanced the immunogenicity and protective efficacy of the rPal antigen, highlighting its potential for practical applications in vaccine development against bacterial infections.

Discussion

The development of subunit vaccines capable of eliciting both humoral and cellular immune responses remains a major challenge in modern vaccinology.[1] In this study, we designed a dual-adjuvant nano-emulsion system, Sq@TA/Mn, which synergistically integrates Sq and Mn^{2+} within a TA/Mn^{2+} coordination network. This platform demonstrated potent efficacy in amplifying antigen-specific immunity, addressing the limitations of conventional adjuvants such as alum, which mainly induce antibody responses but are inefficient at promoting $CD8^+$ T cell activation.

A key feature of the Sq@TA/Mn system lies in its ability to co-deliver both antigen and adjuvant to APCs, while leveraging the distinct immunostimulatory properties of Mn^{2+} and Sq. The TA/Mn^{2+} coordination not only enabled rapid antigen adsorption but also stabilized the nano-emulsion, achieving a high OVA loading efficiency (85.02%) and sustained antigen retention at the injection site for more than six days. This prolonged antigen exposure likely enhanced

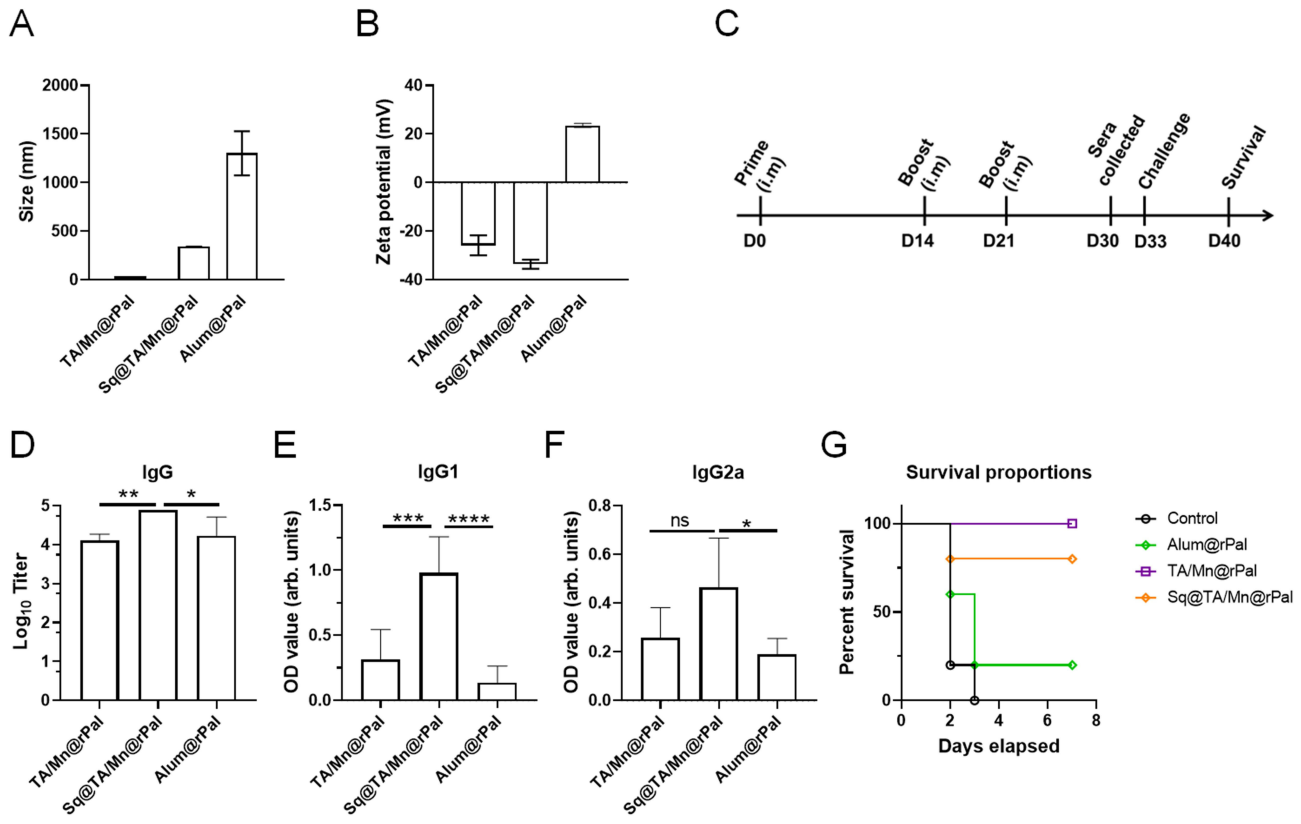

Figure 7 Average size (**A**) and zeta-potential (**B**) of TA/Mn@rPal, Sq@TA/Mn@rPal, and Alum@rPal measured using DLS. (**C**) The schematic outlines the immunization schedule and the overall experimental design. Groups of five C57BL/6 mice were immunized intramuscularly on days 0, 14, and 21 with HEPES, TA/Mn@rPal, Sq@TA/Mn@rPal, or Alum@rPal formulations. Serum samples were collected on day 30 to quantify the titers of total IgG (**D**), IgG1 (**E**), and IgG2a (**F**) specific to rPal. (**E**) and (**F**) were performed at 1:15625 and 1:625 dilutions, respectively. Data in panels (**D**), (**E**), and (**F**) are presented as mean ± SD (n = 5). (**G**) To assess protective efficacy, C57BL/6 mice were intramuscularly vaccinated with the various preparations and subsequently challenged intratracheally with LAC-4 on day 33. Mouse survival was monitored over a 7-day period. All results are shown as mean ± SD (n = 5). Statistical comparisons were performed using the two-tailed unpaired Student's *t*-test. *p < 0.05, **p < 0.01, ***p < 0.001 and ****p < 0.0001. ns, not significant.

and extended APC activation, a prerequisite for durable immunity.[45] Moreover, the pH-dependent stability of the TA/Mn^{2+} network conferred structural stability under physiological conditions while facilitating controlled disassembly in acidic lysosomal environments, potentially promoting efficient antigen cross-presentation.[34]

An intriguing observation relates to the redox activity of Sq. Sq is known to act as a double-edged sword in redox biology: functioning as an antioxidant under moderate oxidative conditions but switching to a pro-oxidant role when oxidative defenses are compromised, due to its highly unsaturated backbone.[22,24] In our study, Sq@TA/Mn@OVA triggered ROS production in DC2.4 cells at concentrations of 6.25 μg/mL Sq and 12.5 μg/mL Mn^{2+}, revealing a context-dependent pro-oxidant effect. This finding provides mechanistic insight into the complex role of Sq in DC activation. To our knowledge, no published studies have directly examined the combined effects of Sq and Mn^{2+} on ROS generation. Individually, Mn^{2+} is well established to promote oxidative stress through mitochondrial dysfunction, particularly at the Complex II ubiquinone-binding site,[55] while Sq can undergo peroxidation to yield pro-oxidant species under certain conditions.[22,56] It is therefore plausible that Mn^{2+}induced ROS may oxidize Sq, generating reactive lipid peroxides that could further amplify oxidative stress. While this interplay remains speculative, it raises an important mechanistic hypothesis for future investigation.

Concerns regarding Mn^{2+}-related toxicity warrant careful consideration. Previous studies have demonstrated that chelation strategies effectively reduce free Mn^{2+} levels and mitigate neurotoxicity.[57] For instance, para-aminosalicylic acid (PAS) lowers manganese concentrations in the brain and cerebrospinal fluid, restoring metal homeostasis in rat models,[58] while agents such as Ethylenediaminetetraacetic acid (EDTA), Diethylenetriaminepentaacetic acid (DTPA), and Nitrilotriacetic acid (NTA) also facilitate manganese clearance.[57] Clinical case report also documents the therapeutic

benefit of PAS in patients with manganese poisoning.[59] In our in vivo experiments, mice immunized with various OVA formulations showed no behavioral abnormalities, weight loss, or histopathological changes in major organs, supporting the systemic safety of Sq@TA/Mn@OVA.

Our data also reinforce the immunopotentiating role of Sq. Prior reports indicate that emulsifying squalene with aluminum hydroxide significantly enhances IgG titers compared with alum alone.[60] Similarly, we observed that Sq@TA/Mn@OVA induced significantly higher IgG titers than TA/Mn@OVA. Notably, we found that there was no significant difference between the Alum@OVA and Sq@TA/Mn@OVA. It is interesting that the IgG titer of Alum@OVA (390,625) was significantly higher than that of Alum@rPal (17,025). Additionally, we noted that the average hydrodynamic diameter of Alum@OVA was 1597.67 nm, which is larger than that of Alum@rPal (1301.67 nm). Although particle size can influence antigen uptake and immune activation,[61] the stronger immune response observed for Alum@OVA compared to Alum@rPal may also be attributed to antigen properties and antigen–adjuvant interactions rather than size alone. Several studies have indicated that physicochemical interactions between alum and protein antigens (such as adsorption efficiency, surface charge, and stability) can critically modulate immune outcomes.[62]

Importantly, translational validation using the rPal antigen from Acinetobacter baumannii confirmed the platform's potential. Consistent with earlier reports that Alum@rPal enhances survival following *A. baumannii* infection,[31] our data demonstrate that Sq@TA/Mn@rPal elicited significantly higher IgG, IgG1, and IgG2a titers compared with alum, resulting in an 80% survival rate against lethal pneumonia challenge versus 20% with Alum@rPal. These findings underscore the superior immunogenicity and protective efficacy of the Sq@TA/Mn system, highlighting its promise as a next-generation vaccine platform against multidrug-resistant pathogens.

In conclusion, this study establishes Sq@TA/Mn as a potent and versatile nano-emulsion adjuvant system that enhances both humoral and cellular immunity. Further mechanistic studies on ROS generation and comprehensive neurotoxicity evaluations are warranted, along with exploration of its applicability to broader disease models such as viral infections and cancer.

Conclusion

We successfully developed a novel nano-emulsion adjuvant platform, Sq@TA/Mn, by incorporating Mn^{2+} and Sq. To validate its immune-enhancing capabilities, the model antigen, OVA, was loaded into the emulsion to create an Sq@TA/Mn@OVA vaccine formulation. Compared with Alum@OVA, the Sq@TA/Mn@OVA vaccine induced stronger OVA-specific humoral and cellular immune responses, as evidenced by higher antibody titers and an increase in IFN-γ production and spleen effector memory T cell population. Remarkably, this also expanded the TRM. Building on this foundation, we evaluated the protective efficacy of the Sq@TA/Mn formulation by incorporating the recombinant antigen rPal to develop a vaccine (Sq@TA/Mn@rPal) against *A. baumannii* pneumonia. The Sq@TA/Mn adjuvant outperformed conventional alum adjuvants, generating more potent Th1/Th2 responses. Importantly, the Sq@TA/Mn@rPal vaccine provided enhanced protection against *A. baumannii* infection, establishing its effectiveness as a bacterial vaccine adjuvant. This study provides a novel method for the co-delivery of dual adjuvants and antigens. Considering the pressing need for safe and efficient vaccine platforms capable of inducing robust humoral and cellular immunity against infectious diseases, we anticipate that the Sq@TA/Mn nano-emulsions will have broad applications in future vaccine development.

Abbreviations

TA, tannic acid; OVA, ovalbumin; DC, dendritic cell; rPal, recombinant peptidoglycan-associated lipoprotein; A. baumannii, Acinetobacter baumannii; PAMPs, pathogen-associated molecular patterns; PRRs, pattern recognition receptors; ROS, reactive oxygen species; Sq, Squalene; APC, antigen-presenting cell; MPNs, metal-phenolic networks; DCFH-DA, dichlorofluorescein-diacetate; FITC, fluorescein isothiocyanate; DMSO, Dimethyl sulfoxide; TEM, transmission electron microscope; STED, Stimulated Emission Depletion; CFU, colony-forming units; DLS, dynamic light scattering; ALP, Alkaline Phosphatase; ALT, Alanine Transaminase; AST, Aspartate Transaminase; LDH, Lactate Dehydrogenase; BUN, Blood Urea Nitrogen; Tem, Effector memory T cells; TRM, Resident memory T cells; PAS, para-

aminosalicylic acid; EDTA, Ethylenediaminetetraacetic acid; DTPA, Diethylenetriaminepentaacetic acid; NTA, Nitrilotriacetic acid.

Acknowledgments

This work was supported by National Natural Science Foundation of China (NSFC) under Grant No. 32270944 and No. 81901865, 1·3·5 project for disciplines of excellence, West China Hospital, Sichuan University under Grant No. ZYXY21004, Sichuan Provincial Science and Technology Program (2025ZNSFSC1744). We thank Dr Howard Xu (California State University Los Angeles, USA) and Wangxue Chen (National Research Council Canada, Canada) for providing the A. baumannii strain. We thank Sisi Wu and Yinchan Wang (Core Facility of West China Hospital, Sichuan University) for their help in the measurements of size and zeta potential of nano-emulsion. We thank Qiuxiao Shi (Core Facility of West China Hospital, Sichuan University) for her assistance of TEM images.

Author Contributions

All authors made a significant contribution to the work reported, whether that is in the conception, study design, execution, acquisition of data, analysis and interpretation, or in all these areas; took part in drafting, revising or critically reviewing the article; gave final approval of the version to be published; have agreed on the journal to which the article has been submitted; and agree to be accountable for all aspects of the work.

Disclosure

The authors report no conflicts of interest in this work.

References

1. Zhang Y, Xu J-C, Hu Z-D, Fan X-Y. Advances in protein subunit vaccines against tuberculosis. *Front Immunol*. 2023;14:1238586. doi:10.3389/fimmu.2023.1238586
2. Khalili S, Chen W, Jahangiri A. Editorial: recent advances in the development of vaccines against Acinetobacter baumannii. *Front Immunol*. 2023;14:1187554. doi:10.3389/fimmu.2023.1187554
3. Bao W, Zhang Y, Shang C, et al. Supramolecular lipopeptidic adjuvant regulates protective abilities of MPXV subunit vaccine against monkeypox virus. *Chem Eng J*. 2025;507:160670. doi:10.1016/j.cej.2025.160670
4. He T, Liang X, Li L, et al. A spontaneously formed and self-adjuvanted hydrogel vaccine triggers strong immune responses. *Mater Des*. 2021;197:109232. doi:10.1016/j.matdes.2020.109232
5. Moyle PM, Toth I. Modern subunit vaccines: development, components, and research opportunities. *ChemMedChem*. 2013;8(3):360–376. doi:10.1002/cmdc.201200487
6. Mascola JR, Fauci AS. Novel vaccine technologies for the 21st century. *Nat Rev Immunol*. 2020;20(2):87–88. doi:10.1038/s41577-019-0243-3
7. Shrimali PC, Chen S, Das A, et al. Amyloidogenic propensity of self-assembling peptides and their adjuvant potential for use as DNA vaccines. *Acta Biomater*. 2023;169:464–476. doi:10.1016/j.actbio.2023.08.015
8. Gutjahr A, Tiraby G, Perouzel E, Verrier B, Paul S. Triggering intracellular receptors for vaccine adjuvantation. *Trends Immunol*. 2016;37(9):573–587. doi:10.1016/j.it.2016.07.001
9. Hou Y, Wang Y, Tang Y, et al. Co-delivery of antigen and dual adjuvants by aluminum hydroxide nanoparticles for enhanced immune responses. *J Control Release*. 2020;326:120–130. doi:10.1016/j.jconrel.2020.06.021
10. Gao Z-L, Xu W, Zheng S-J, Duan Q-J, Liu R, Du J-Z. Orchestrated cytosolic delivery of antigen and adjuvant by manganese ion-coordinated nanovaccine for enhanced cancer immunotherapy. *Nano Lett*. 23(5):1904–1913. doi:10.1021/acs.nanolett.2c04970
11. Zhang R, Wang C, Guan Y, et al. Manganese salts function as potent adjuvants. *Cell Mol Immunol*. 2021;18(5):1222–1234. doi:10.1038/s41423-021-00669-w
12. Shi P-D, Xu Y-P, Zhu Z, et al. Manganese mineralization of pathogenic viruses as a universal vaccine platform. *Adv Sci*. 2023;10(33):2303615. doi:10.1002/advs.202303615
13. Qiao N, Wang H, Xu Y, et al. A MnAl double adjuvant nanovaccine to induce strong humoral and cellular immune responses. *J Control Release*. 2023;358:190–203. doi:10.1016/j.jconrel.2023.04.036
14. Chen K, Wang N, Zhang X, Wang M, Liu Y, Shi Y. Potentials of saponins-based adjuvants for nasal vaccines. *Front Immunol*. 2023;14:1153042. doi:10.3389/fimmu.2023.1153042
15. Yildiz S, Alpdundar E, Gungor B, et al. Enhanced immunostimulatory activity of cyclic dinucleotides on mouse cells when complexed with a cell-penetrating peptide or combined with CpG. *Eur J Immunol*. 2015;45(4):1170–1179. doi:10.1002/eji.201445133
16. Li Y, Chen Z, Lu X, et al. STING and TLR9 agonists synergistically enhance the immunogenicity of SARS-CoV-2 subunit vaccine. *Nano Res*. 2023;16(12):13322–13334. doi:10.1007/s12274-023-6295-5
17. Qin T, Ma S, Miao X, et al. Mucosal vaccination for influenza protection enhanced by catalytic immune-adjuvant. *Adv Sci*. 2020;7(18):2000771. doi:10.1002/advs.202000771
18. Huang CH, Huang CY, Huang MH. Unsaturated squalene content in emulsion vaccine adjuvants plays a crucial role in ROS-mediated antigen uptake and cellular immunity. *Mol Pharm*. 2018;15(2):420–429. doi:10.1021/acs.molpharmaceut.7b00800

19. Goepfert PA, Fu B, Chabanon A-L, et al. Safety and immunogenicity of SARS-CoV-2 recombinant protein vaccine formulations in healthy adults: interim results of a randomised, placebo-controlled, Phase 1-2, dose-ranging study. *Lancet Infect Dis*. 2021;21(9):1257–1270. doi:10.1016/S1473-3099(21)00147-X
20. Leroux-Roels I, Borkowski A, Vanwolleghem T, et al. Antigen sparing and cross-reactive immunity with an adjuvanted rH5N1 prototype pandemic influenza vaccine: a randomised controlled trial. *Lancet*. 2007;370(9587):580–589. doi:10.1016/S0140-6736(07)61297-5
21. Lou-Bonafonte JM, Martínez-Beamonte R, Sanclemente T, et al. Current insights into the biological action of squalene. *Mol Nutr Food Res*. 2018;62(15):1800136. doi:10.1002/mnfr.201800136
22. Shimizu N, Ito J, Kato S, et al. Oxidation of squalene by singlet oxygen and free radicals results in different compositions of squalene monohydroperoxide isomers. *Sci Rep*. 2018;8(1):9116. doi:10.1038/s41598-018-27455-5
23. Kohno Y, Egawa Y, Itoh S, S-i N, Takahashi M, Mukai K. Kinetic study of quenching reaction of singlet oxygen and scavenging reaction of free radical by squalene in n-butanol. *Biochim Biophys Acta, Lipids Lipid Metab*. 1995;1256(1):52–56. doi:10.1016/0005-2760(95)00005-W
24. Palaniyandi T, Sivaji A, Thiruganasambandam R, Natarajan S, Hari R. In vitro antigastric cancer activity of squalene, a triterpenoid compound isolated from Rhizophora mucronata mangrove plant leaves against AGS cell line. *Phcog Mag*. 2018;14(57s). doi:10.5555/20183375924
25. Liu G, Zhu M, Zhao X, Nie G. Nanotechnology-empowered vaccine delivery for enhancing $CD8^+$ T cells-mediated cellular immunity. *Adv Drug Deliv Rev*. 2021;176:113889. doi:10.1016/j.addr.2021.113889
26. Lu Y, Zeng T, Zhang H, et al. Nano-immunotherapy for lung cancer. *Nano TransMed*. 2023;2(1):e9130018. doi:10.26599/NTM.2023.9130018
27. Han Y, Zhou J, Hu Y, et al. Polyphenol-based nanoparticles for intracellular protein delivery via competing supramolecular interactions. *ACS Nano*. 2020;14(10):12972–12981. doi:10.1021/acsnano.0c04197
28. Wu D, Zhou B, Wang S, Pei Y, Li B, Liang H. Pickering emulsion stabilized by metal-phenolic architectures: a straightforward in situ assembly strategy. *J Agric Food Chem*. 2021;69(39):11709–11719. doi:10.1021/acs.jafc.1c02066
29. Janes ME, Gottlieb AP, Park KS, Acharya S, Bibbey MG, Mitragotri S. Controlling vaccine kinetics using tannic acid for enhanced humoral immunity. *J Control Release*. 2025;379:135–146. doi:10.1016/j.jconrel.2024.12.054
30. Cabral-Hipólito N, Molina-Ramírez BS, Castillo-Maldonado I, et al. Tannic acid exhibits adjuvant activity by enhancing humoral and cell-mediated immunity against BSA as a protein antigen. *Protein Pept Lett*. 2022;29(2):166–175. doi:10.2174/0929866528666211125110701
31. Zeng X, Wang N, Xiang C, et al. Peptidoglycan-associated lipoprotein contributes to the virulence of Acinetobacter baumannii and serves as a vaccine candidate. *Genomics*. 2023;115(2):110590. doi:10.1016/j.ygeno.2023.110590
32. Harris G, Lee RK, Lam CK, et al. A mouse model of acinetobacter baumannii-associated pneumonia using a clinically isolated hypervirulent strain. *Antimicrob Agents Chemother*. 2013;57(8):3601–3613. doi:10.1128/aac.00944-13
33. Besford QA, Ju Y, Wang TY, et al. Self-Assembled metal-phenolic networks on emulsions as low-fouling and pH-responsive particles. *Small*. 2018;14(39):e1802342. doi:10.1002/smll.201802342
34. Guo J, Ping Y, Ejima H, et al. Engineering multifunctional capsules through the assembly of metal–phenolic networks. *Angew Chem Int Ed*. 2014;53(22):5546–5551. doi:10.1002/anie.201311136
35. Ejima H, Richardson JJ, Liang K, et al. One-step assembly of coordination complexes for versatile film and particle engineering. *Science*. 2013;341(6142):154–157. doi:10.1126/science.1237265
36. Feng Q, Cheng K, Zhang L, et al. Rationally designed multimeric nanovaccines using icosahedral DNA origami for display of SARS-CoV-2 receptor binding domain. *Nat Commun*. 2024;15(1):9581. doi:10.1038/s41467-024-53937-4
37. Wang N, Wang D, Xing K, et al. Ultrasonic treatment of rice bran protein-tannic acid stabilized oil-in-water emulsions: focus on microstructure, rheological properties and emulsion stability. *Ultrason Sonochem*. 2023;99:106577. doi:10.1016/j.ultsonch.2023.106577
38. Matsue H, Edelbaum D, Shalhevet D, et al. Generation and function of reactive oxygen species in dendritic cells during antigen presentation1. *J Immunol*. 2003;171(6):3010–3018. doi:10.4049/jimmunol.171.6.3010
39. Li J, Deng C, Liang W, et al. Mn-containing bioceramics inhibit osteoclastogenesis and promote osteoporotic bone regeneration via scavenging ROS. *Bioact Mater*. 2021;6(11):3839–3850. doi:10.1016/j.bioactmat.2021.03.039
40. Song C, Li F, Wang S, Wang J, Wei W, Ma G. Recent advances in particulate adjuvants for cancer vaccination. *Adv Ther*. 2020;3(5):1900115. doi:10.1002/adtp.201900115
41. Wang S, Ni D, Yue H, et al. Exploration of antigen induced $CaCO_3$ nanoparticles for therapeutic vaccine. *Small*. 2018;14(14):1704272. doi:10.1002/smll.201704272
42. Silverman J. Clinical biochemistry parameters in C57BL/6J mice after blood collection from the submandibular vein and retroorbital plexus. *J Am Assoc Lab Anim Sci*. 2010;49(4):400. doi:10.1016/j.jdsci.2009.11.010
43. Li M, Liang Z, Chen C, et al. Virus-like particle-templated silica-adjuvanted nanovaccines with enhanced humoral and cellular immunity. *ACS Nano*. 2022;16(7):10482–10495. doi:10.1021/acsnano.2c01283
44. Liu X, Chen S, Huang J, et al. Synthetic polypeptides inhibit nucleic acid-induced inflammation in autoimmune diseases by disrupting multivalent TLR9 binding to LL37-DNA bundles. *Nat Nanotechnol*. 2024. doi:10.1038/s41565-024-01759-2
45. Chen M-C, Huang S-F, Lai K-Y, Ling M-H. Fully embeddable chitosan microneedles as a sustained release depot for intradermal vaccination. *Biomaterials*. 2013;34(12):3077–3086. doi:10.1016/j.biomaterials.2012.12.041
46. Toor SM, Saleh R, Sasidharan Nair V, Taha RZ, Elkord E. T-cell responses and therapies against SARS-CoV-2 infection. *Immunology*. 2021;162(1):30–43. doi:10.1111/imm.13262
47. Krishnan L, Gurnani K, Dicaire CJ, et al. Rapid clonal expansion and prolonged maintenance of memory $CD8^+$ T cells of the effector (CD44highCD62Llow) and central (CD44highCD62Lhigh) phenotype by an archaeosome adjuvant independent of TLR2. *J Immunol*. 2007;178(4):2396–2406. doi:10.4049/jimmunol.178.4.2396
48. Rotrosen E, Kupper TS. Assessing the generation of tissue resident memory T cells by vaccines. *Nat Rev Immunol*. 2023;23(10):655–665. doi:10.1038/s41577-023-00853-1
49. Sallusto F, Geginat J, Lanzavecchia A. Central memory and effector memory T cell subsets: function, generation, and maintenance. *Annu Rev Immunol*. 2004;22:745–763. doi:10.1146/annurev.immunol.22.012703.104702
50. Zhang K, Qi C, Cai K. Manganese-based tumor immunotherapy. *Adv Mater*. 2023;35(19):2205409. doi:10.1002/adma.202205409
51. Yuan R, Yu J, Jiao Z, et al. The roles of tissue-resident memory T cells in lung diseases. *Front Immunol*. 2021;12:710375. doi:10.3389/fimmu.2021.710375

52. Iwanaga N, Chen K, Yang H, et al. Vaccine-driven lung TRM cells provide immunity against Klebsiella via fibroblast IL-17R signaling. *Sci Immunol*. 2021;6(63):eabf1198. doi:10.1126/sciimmunol.abf1198
53. Auladell M, Jia X, Hensen L, et al. Recalling the future: immunological memory toward unpredictable influenza viruses. *Front Immunol*. 2019;10:1400. doi:10.3389/fimmu.2019.01400
54. Chen W. Host Innate Immune Responses to Acinetobacter baumannii Infection. *Front Cell Infect Microbiol*. 2020;10:486. doi:10.3389/fcimb.2020.00486
55. Bonke E, Zwicker K, Dröse S. Manganese ions induce H_2O_2 generation at the ubiquinone binding site of mitochondrial complex II. *Arch Biochem Biophys*. 2015;580:75–83. doi:10.1016/j.abb.2015.06.011
56. Cárdeno A, Aparicio-Soto M, Montserrat-de la paz S, Bermudez B, Muriana FJG, Alarcón-de-la-lastra C. Squalene targets pro- and anti-inflammatory mediators and pathways to modulate over-activation of neutrophils, monocytes and macrophages. *J Funct Foods*. 2015;14:779–790. doi:10.1016/j.jff.2015.03.009
57. Blanusa M, Varnai VM, Piasek M, Kostial K. Chelators as antidotes of metal toxicity: therapeutic and experimental aspects. *Curr Med Chem*. 2005;12(23):2771–2794. doi:10.2174/092986705774462987
58. Zheng W, Jiang Y-M, Zhang Y, Jiang W, Wang X, Cowan DM. Chelation therapy of manganese intoxication with para-aminosalicylic acid (PAS) in Sprague–Dawley rats. *NeuroToxicology*. 2009;30(2):240–248. doi:10.1016/j.neuro.2008.12.007
59. Jiang Y-M, Mo X-A, Du F-Q, et al. Effective treatment of manganese-induced occupational parkinsonism with p-aminosalicylic acid: a case of 17-year follow-up study. *J Occup Environ Med*. 2006;48(6):644–649. doi:10.1097/01.jom.0000204114.01893.3e
60. Peng S, Cao F, Xia Y, et al. Particulate alum via pickering emulsion for an enhanced COVID-19 vaccine adjuvant. *Adv Mater*. 2020;32(40):2004210. doi:10.1002/adma.202004210
61. Baranov MV, Kumar M, Sacanna S, Thutupalli S, van den Bogaart G. Modulation of immune responses by particle size and shape. *Front Immunol*. 2021;11:607945. doi:10.3389/fimmu.2020.607945
62. Ren H, Jia W, Xie Y, Yu M, Chen Y. Adjuvant physiochemistry and advanced nanotechnology for vaccine development. *Chem Soc Rev*. 2023;52(15):5172–5254. doi:10.1039/D2CS00848C